fluids

MDPI

Article

Experimental and Mechanistic Study on Immersion Behavior of Heterogeneous Particle Beds

Kaifeng Li [1], Lijuan Zhang [1,*], Lu Wang [1], Yuechen Xu [1], Minxin Tang [1], Panmin Guo [1], Jiayi Li [1] and Jos J. Derksen [2]

[1] School of Chemistry and Chemical Engineering, Shanghai University of Engineering Science, Shanghai 201620, China; a3576645199@126.com (K.L.); m18640220742@163.com (L.W.); 18018871208@163.com (Y.X.); tmx2023@126.com (M.T.); 18545839146@163.com (P.G.); jayee0307@163.com (J.L.)

[2] School of Engineering, University of Aberdeen, King's College, Aberdeen AB24 3UE, UK; jderksen@abdn.ac.uk

* Correspondence: zhanglj0128@126.com

Abstract

This study experimentally investigates the immersion behavior of steel and titanium cylinders in spherical and cylindrical heterogeneous particle beds saturated by a Newtonian liquid. The effects of cylinder density, different particle-bed systems, liquid viscosity, bed solid volume fraction, and intruding cylinder aspect ratio on immersion depth are systematically analyzed. Particle trajectories in liquid-saturated beds are recorded using a digital camera at 100 frames per second (fps) and are analyzed by image-processing techniques. Related particle-resolved simulation studies are conducted to support the mechanistic interpretation. Results show that particles with higher density tend to achieve greater immersion depths due to their larger gravitational driving force. Compared with spherical beds, cylindrical beds exhibit different immersion responses depending on liquid viscosity and experimental conditions. In the selected viscosity-comparison cases, the spherical bed gives a larger immersion depth than the cylindrical bed under the lower-viscosity condition, whereas the cylindrical bed gives a larger immersion depth under the higher-viscosity condition. Compacting the bed increases its solid volume fraction, thereby increasing resistance and reducing immersion depth.

Keywords: heterogeneous particle bed; cylindrical intruder; immersion behavior; liquid viscosity; solid volume fraction

1. Introduction

Heterogeneous particle beds consist of different components, including solid particles and interstitial liquid, and their characteristics can vary with the properties of both particles and liquid phases. Differences in particle morphology and liquid properties among the particle-bed systems result in variations in packing structures and pore networks, which affect local resistance, fluid flow, and the motion of intruder particles within the bed [1]. In liquid-saturated beds, these effects become coupled with fluid viscosity and density, making immersion depth dependent on both bed structure and liquid properties [2].

Packed particle beds are widely used in separation and filtration processes and can be regarded as heterogeneous porous media. Their internal packing structure and pore geometry strongly influence fluid flow and particle transport behavior [3]. In many practical processes involving particle transport and processing, intruder particles may enter, migrate, or settle within liquid-saturated porous structures. Understanding particle immersion behavior in liquid-saturated beds is important for predicting particle transport and controlling particle–fluid–bed interactions in complex multiphase systems. However, the mechanism

Check for updates

Academic Editors: Rey Cheng Chin and Abraham Medina

Received: 17 September 2026
Revised: 13 October 2026
Accepted: 22 October 2026
Published: 27 October 2026

Copyright: © 2026 by the authors. Licensee MDPI, Basel, Switzerland. This article is an open access article distributed under the terms and conditions of the Creative Commons Attribution (CC BY) license.

of particle immersion in heterogeneous packed beds under coupled conditions remains insufficiently understood, particularly when considering variations in bed particle shape, bed morphology, and fluid properties [4]. This motivates the present study, which systematically investigates particle immersion behavior in liquid-saturated heterogeneous beds.

Particle impact and penetration in dry granular beds are widely studied, focusing on impact dynamics, immersion depth, crater formation, and resistance mechanisms [5–7]. The influence of interstitial fluids is also examined in wet granular systems, where liquid content and fluid-mediated interactions can significantly affect immersion behavior [4,8,9]. Related studies on cylindrical particles and wet granular beds further provide reference for understanding particle intrusion in liquid-saturated beds [10,11].

Despite these studies, the coupled effects of bed-particle shape, intruder properties, solid volume fraction, and liquid viscosity on immersion behavior remain insufficiently understood [4,5,8,11]. Existing studies mainly consider relatively simple bed structures or limited parameter combinations [5,8,11]. Therefore, further experimental evidence is needed to clarify how particle, bed, and fluid properties jointly control immersion depth in liquid-saturated heterogeneous particle beds.

This study experimentally investigates the immersion behavior of steel and titanium cylindrical intruders in liquid-saturated heterogeneous particle beds composed of spherical or cylindrical bed particles. The effects of intruder density, intruder aspect ratio, different particle-bed systems, solid volume fraction, and liquid viscosity on immersion depth are systematically examined. The objective is to clarify how intruder properties, liquid characteristics, particle-bed morphology, and packing state jointly influence immersion behavior and to provide experimental evidence for understanding particle–bed–fluid interactions in heterogeneous packed beds.

2. Materials and Methods

2.1. Experimental Materials

The experimental materials are made up of three main parts: bed particles, intruder particles, and interstitial liquids. The experimental system is similar to that reported in [11]. For the bed particles, two types of regular acrylic particles are used: spherical acrylic particles with a diameter of 2.00 ± 0.05 mm and cylindrical acrylic particles with a diameter of 1.75 ± 0.05 mm and a length of 1.50 ± 0.05 mm. Both types of acrylic bed particles are supplied by Baoji Boze Metal Products Co., Ltd. (Baoji, Shaanxi, China), as summarized in Table 1. The density of the acrylic particles was measured as 1250 ± 13 kg/m^3 for spherical particles and 1250 ± 12 kg/m^3 for cylindrical particles, based on repeated mass–volume measurements. In order to facilitate scale comparison with the spherical particles, the cylindrical bed particles can be converted into an equivalent spherical diameter, following the principle of equal volume: $d_e = \sqrt[3]{\frac{3d_c^2 l_c}{2}}$. Here, d_c is the diameter of the cylindrical bed particle, and l_c is its length. Based on the measured dimensions of the cylindrical bed particles, the equivalent spherical diameter calculated from the equal-volume principle is $d_e = 1.90 \pm 0.05$ mm.

Table 1. Bed particles.

Bed Particle	Spherical Particle, Acrylic	Cylindrical Particle, Acrylic
Diameter (mm)	2.00 ± 0.05	1.75 ± 0.05
Length (mm)		1.5 ± 0.05
Density (kg/m^3)	1250 ± 13	1250 ± 12

For the intruder particles, steel and titanium cylindrical particles supplied by Baoji Boze Metal Products Co., Ltd. (Baoji, Shaanxi, China) are employed. Their diameters are all 4.00 ± 0.05 mm, while their lengths are 4.00 ± 0.05 mm, 8.00 ± 0.05 mm, 12.00 ± 0.05 mm, and 16.00 ± 0.05 mm, respectively. This corresponds to aspect ratios $\frac{l_a}{d_a}$ of 1, 2, 3, and 4, respectively. The density of steel particles is 7850 ± 79 kg/m^3, while that of titanium particles is 4500 ± 45 kg/m^3, as shown in Table 2. These particles have regular dimensions and distinctly different densities, allowing the effect of intruder density on the final immersion depth to be examined.

Table 2. Intruder particles.

Material	Steel	Titanium
Density (kg/m^3)	7850 ± 79	4500 ± 45
Diameter (mm)	4.00 ± 0.05	
Length (mm)	4.00, 8.00, 12.00, 16.00 (each ± 0.05)	

Four types of Newtonian fluids are selected to serve as the interstitial liquids, which include a 50% glycerol–water solution, a 30% glycerol–water–sodium chloride (NaCl) solution, a 19% NaCl aqueous solution, as well as a polyethylene glycol (PEG) aqueous solution. Analytical-grade glycerol, sodium chloride, and polyethylene glycol are purchased from Shanghai Aladdin Biochemical Technology Co., Ltd. (Shanghai, China). The experimental temperature is controlled at 24 ± 1 °C. The dynamic viscosity of each liquid is measured using an NDJ-5S rotational viscometer (Shanghai Fangrui Instrument Co., Ltd., Shanghai, China), while the liquid density is measured using a pycnometer (Shanghai Heqi Glassware Co., Ltd., Shanghai, China). The mass of the liquid is obtained by subtracting the empty pycnometer mass from the filled pycnometer mass, and the density is calculated by dividing the measured liquid mass by the calibrated pycnometer volume. The uncertainties of the viscosity and density measurements are estimated according to the manufacturers' specified instrument accuracies and are reported as absolute uncertainties together with the measured density and dynamic viscosity values in Table 3. The 19% NaCl solution, 30% glycerol–water–NaCl solution, and 50% glycerol–water solution have similar densities but different viscosities, allowing immersion behavior to be compared under different viscosity conditions. The PEG aqueous solution and 50% glycerol–water solution have similar viscosities but different densities, allowing immersion behavior to be compared under different density conditions.

Table 3. Liquids. Abbreviations: NaCl, sodium chloride; PEG, polyethylene glycol.

Liquid, Newtonian Fluid at 24 ± 1 °C	50% Glycerol–Water	30% Glycerol–Water–NaCl	19% NaCl Solution	PEG Aqueous Solution
Density (kg/m^3)	1137 ± 11	1136 ± 11	1136 ± 11	1051 ± 11
Viscosity (mPa·s)	8.55 ± 0.09	5.70 ± 0.06	3.10 ± 0.03	8.36 ± 0.08

2.2. Experimental Apparatus and Equipment

The core apparatus is a transparent acrylic container made from optical-grade acrylic plates by Shanghai Qiankai Marine Engineering Co., Ltd. (Shanghai, China), offering high transmittance and low optical distortion. The imaging system records the complete motion and displacement evolution of intruding particles from the side, as shown in Figure 1.

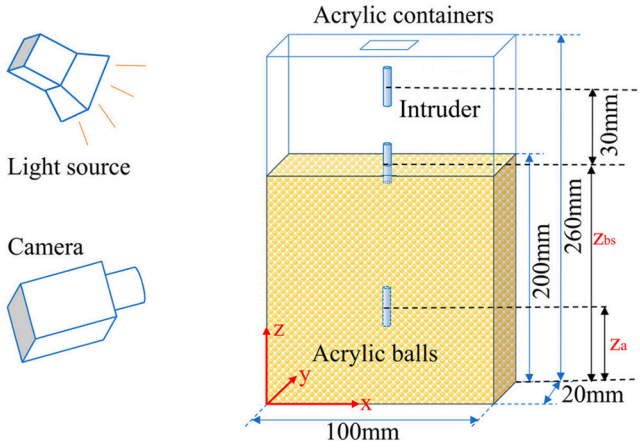


Figure 1. Schematic diagram of the experimental setup.

The container has a rectangular open-top structure, with internal dimensions of 100 mm × 20 mm × 260 mm. To support image acquisition and spatial calibration, the front and rear acrylic walls are polished. Standard grid calibration paper with 5 mm squares is attached to the outer wall to convert image pixels into physical scale. A 3 mm thick matte white diffuse-reflection plate is mounted behind the container to reduce background stray light and spot interference, thereby improving imaging contrast between intruding and bed particles. These settings provide a high-quality image basis for trajectory extraction and data analysis.

To capture the transient displacement evolution of intruding particles in liquid-saturated beds, a Sony Handycam FDR-AX700 digital video camera recorder (Sony Corporation, Tokyo, Japan) equipped with an LED flat-panel light source is used for image acquisition. Videos are recorded at a frame rate of 100 frames per second (fps) with a spatial resolution of 1920 × 1080 pixels. The uniform LED illumination minimizes background shadows and enhances the contrast between the intruding particle and the surrounding bed particles, thereby facilitating subsequent trajectory extraction and image analysis.

After image data from the immersion process are exported, MATLAB (R2024a; The MathWorks, Inc., Natick, MA, USA)-based background subtraction and centroid-tracking algorithms are used for subsequent data processing [11].

2.3. Experimental Procedure

The four transparent saturated liquids (see Table 3) are prepared using deionized water as solvent. Analytical-grade reagents are used to ensure stable physical properties and good experimental repeatability.

Spherical acrylic beads and cylindrical acrylic beads are first soaked in deionized water and ethanol for cleaning. After thorough washing, the particles are placed on stainless-steel trays and dried naturally for 12 h in a clean environment at 25 ± 2 °C with dust protection. Finally, the dried particles are sealed for storage.

A prescribed mass of the dried bed particles is weighed before loading and poured into the empty acrylic container described in Section 2.2. One of the prepared liquids is then slowly introduced along the inner wall of the container. A glass guide rod is used to stabilize the inflow, and the filling rate is gradually reduced as the liquid level rises. During saturation, the particle bed is gently disturbed using a glass rod to facilitate the release of air in the spaces, allowing the saturated bed to settle naturally. Liquid addition is continued until the liquid level, measured from the bottom of the container, reaches 230 mm. The saturated particle bed is then allowed to settle naturally until no further change in bed

height is observed. Under this naturally settled condition, the bed height stabilizes at 200 mm, leaving a 30 mm liquid column above the bed.

The solid volume fraction of the bed is determined before liquid saturation. It is defined as $\varphi = \frac{V_s}{V_{bed}}$, where V_s is the total volume of solid bed particles and V_{bed} is the total volume occupied by the particle bed, including interstitial voids. For each bed type, the mass of particles filled into the container is measured, and V_s is calculated from the measured particle mass and the corresponding material density. V_{bed} is calculated from the container base area and the measured bed height.

The uncertainty of the solid volume fraction was evaluated using first-order propagation of uncertainty:

$$\frac{\Delta\varphi}{\varphi} = \sqrt{\left(\frac{\Delta m_p}{m_p}\right)^2 + \left(\frac{\Delta\rho_p}{\rho_p}\right)^2 + \left(\frac{\Delta A}{A}\right)^2 + \left(\frac{\Delta H}{H}\right)^2} \quad (1)$$

where m_p, ρ_p, A, and H represent the particle mass, particle density, container base area, and bed height, respectively. The relative uncertainties associated with particle density were 1.04% for spherical particles and 0.96% for cylindrical particles. The uncertainties associated with particle mass, container dimensions, and bed height were evaluated based on instrument accuracy and repeated measurements. The resulting relative uncertainties of these quantities were all within 1%.

The combined relative uncertainty of the solid volume fraction was approximately 2.0%, resulting in absolute uncertainties of ± 0.012 and ± 0.011 for the spherical-particle and cylindrical-particle beds, respectively. Under the natural settling and gentle tapping procedure used in the main experiments, the initial solid volume fractions are $\varphi = 0.590 \pm 0.012$ for the spherical-particle bed and $\varphi = 0.543 \pm 0.011$ for the cylindrical-particle bed. For the compaction test, the cylindrical-particle bed is first prepared under the same natural settling procedure and is then further compacted by vibration until no further decrease in bed height is observed. This compaction reduces the bed height from 200 mm to approximately 195 mm and increases the solid volume fraction from $\varphi = 0.543 \pm 0.011$ to $\varphi = 0.557 \pm 0.011$. A similar compaction procedure is also applied to the saturated spherical-particle bed, where the bed height decreases from 200 mm to approximately 195 mm and the solid volume fraction increases from $\varphi = 0.590 \pm 0.012$ to $\varphi = 0.605 \pm 0.012$. The naturally settled beds are used for the main experiments examining the effects of liquid properties, bed-particle morphology, intruder material, and intruder aspect ratio, whereas the compacted cylindrical bed is used only for the additional solid-volume-fraction comparison experiments.

All combinations of intruding-particle material, aspect ratio, saturated liquid, and bed type are tested, including 4 liquids × 2 bed types × 2 intruder materials × 4 lengths, giving 64 working conditions. Each condition is independently repeated three times, and the immersion-depth results are reported as the mean ± standard deviation.

A stainless-steel tweezer is used to clamp the upper end of the cylindrical intruder and suspend it above the bed. The intruder center is aligned with the bed center, with the lateral release-position deviation controlled within approximately ±1 mm. The release height is defined as the vertical distance between the initial geometric center of the intruder and the undisturbed bed surface immediately before release. For the homogeneous cylindrical intruders used here, the geometric center coincides with the center of mass. The release height is set to 30 ± 1 mm. The cylinder is released with its axis approximately vertical, and the initial projected angle between the cylinder axis and the vertical direction is controlled within approximately 5°, as evaluated from the first video frame before release. The particle is then released to fall freely through the liquid column and penetrate into the granular bed, as shown in Figure 2.

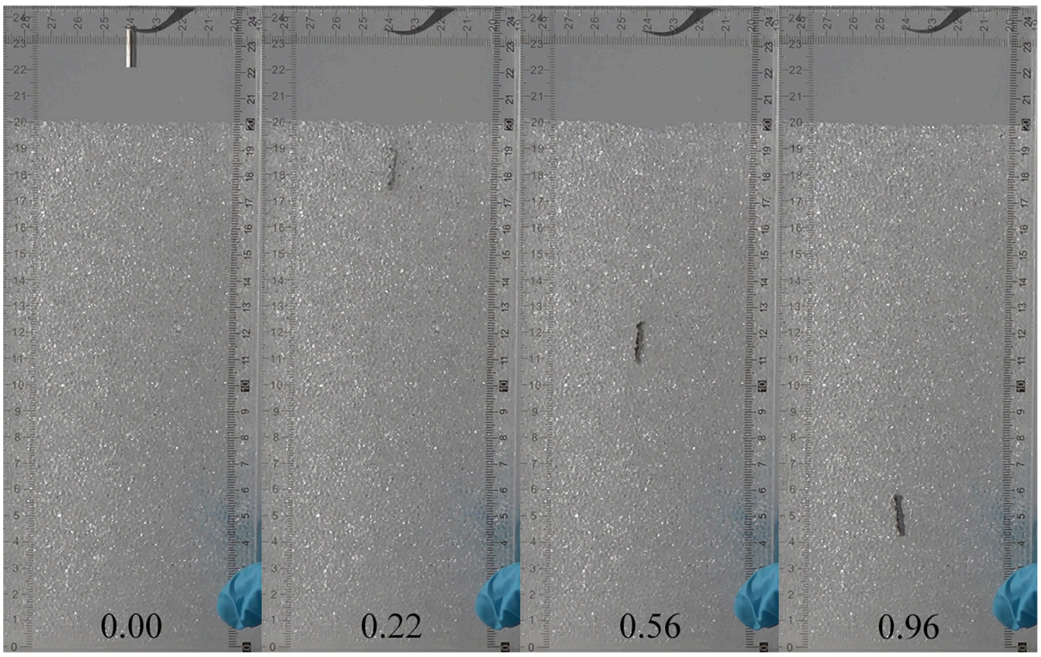


Figure 2. Snapshots of the immersion process of a stainless-steel cylindrical intruder with a diameter of 4 mm and a length of 16 mm in a spherical-particle bed saturated with polyethylene glycol (PEG) solution. Each image is labeled with the corresponding dimensionless time.

To account for scaling effects of liquid viscosity ν and bed particle equivalent diameter d_b, both time and displacement are nondimensionalized. The dimensionless time is defined as:

$$\tau = \frac{(t \cdot \nu)}{{d_b}^2} \tag{2}$$

where ν is kinematic viscosity ($\nu = \eta/\rho$, m^2/s), and d_b is equivalent particle diameter (sphere: 2.0 mm; cylinder converted by equal-volume sphere diameter $d_b = \sqrt[3]{\frac{3d_c^2 l_c}{2}} = 1.90$ mm). This dimensionless time is used to normalize the temporal evolution of particle motion under different viscosity conditions.

Recording is started before manual release to ensure that the complete process from release to final rest is captured. For each trial, approximately 5 s of video is retained for analysis, including at least 0.5 s before the visually identified release moment to cover the initial release, free fall, impact, and immersion stages. Recording is continued for at least 2 s after the intruder reaches its final resting position to ensure complete temporal data for trajectory and immersion-depth analysis. Each condition includes three repeated tests. All videos are first screened to remove invalid samples with operational errors, external disturbance, or imaging defects. Qualified videos are required to show clear particle contours and complete motion paths without obvious blur, overexposure, or underexposure. Because manual release may cause lateral deviation, only videos in which the particle contour is clear, the motion path is complete, and the trajectory does not obviously deviate from the imaging plane are used for subsequent analysis.

The main sources of experimental uncertainty are the release height, lateral release deviation, initial cylinder orientation, and image-based centroid extraction. The uncertainties associated with release height, lateral release deviation, and initial orientation are quantified from the calibrated images before release, while the uncertainty in immersion depth is estimated from repeated tests and image-processing accuracy. The combined relative uncertainty of the final immersion depth is within 5%.

2.4. Data Acquisition and Processing

Video data are exported in a lossless format and processed in MATLAB using a previously reported image-processing method [11]. Each frame is converted to 8-bit grayscale and cropped to remove invalid regions. Adaptive thresholding separates intruding particles from background and bed particles, producing binary images. Morphological closing fills internal voids and removes noise caused by reflection or shadow. The centroid of white pixels is computed as particle position $z(t)$, where t is time from release. The vertical origin is set at the container bottom, with positive z upward (see Figure 1).

Pixel-coordinate sequences and calibration parameters exported from Adobe Photoshop 2024 (Version 25.x; Adobe Inc., San Jose, CA, USA) are then processed in a MATLAB program. The *VideoReader* function reads each selected video frame by frame and converts it into grayscale images. Otsu global thresholding or adaptive local thresholding using the *adaptthresh* function is used to separate the intruding particle from the background and bed particles [12], producing binary images. Morphological closing with a 3-pixel radius fills small holes in the particle region, and the *imfill* function fills internal cavities to keep the particle region complete. The *regionprops* function calculates the centroid coordinates of the particle region in pixels, which are converted into physical coordinates in mm using the calibrated pixel scale and recorded as $z(t)$ and lateral displacement $x(t)$. A Savitzky–Golay filter is applied to the centroid series to remove noise and obtain a smooth displacement–time curve $z(t)$ [13]. Previous studies use similar image-based particle tracking and visualization methods on particle settling and wet granular-bed intrusion [11,14,15].

Figure 3 shows a representative example of the image-processing procedure, including background correction, binary segmentation, and final identification of the intruding cylindrical particle. The masked background-subtracted image is first obtained to reduce interference from the container boundaries and scale marks. The intruder is then separated from the background using thresholding and morphological filtering. The detected boundary and centroid are superimposed on the original frame to visually verify that the identified region corresponds to the intruding cylindrical particle. The shape of the detected boundary is determined by the thresholding and morphological processing results of the binary particle region and is used only for centroid calculation and particle-position extraction rather than representing the exact geometric contour of the intruder.

Each recorded frame is spatially calibrated using the reference scale attached to the acrylic container. As shown in Figure 4, a physical length of 1 cm on the calibration scale corresponds to 40 pixels in the recorded images. Therefore, the measured pixel displacement of the particle centroid is converted into physical displacement using the calibrated scale. The spatial resolution is estimated as 0.25 mm pixel^{-1}, with a calibration uncertainty of approximately $\pm$0.01 mm pixel^{-1}, based on repeated measurements of a 1 cm interval on the reference scale. This calibration procedure ensures consistent conversion between image coordinates and physical coordinates throughout all experiments.

After trajectory extraction, MATLAB outputs structured data containing falling time and immersion depth. The bed surface position Z_{bed} is defined as the mean upper surface height before impact, obtained from three transverse positions: 30 mm from the left wall, the centerline, and 30 mm from the right wall. Final immersion depth is defined as:

$$D = Z_{\text{bed}} - Z_{\text{final}} \tag{3}$$

where Z_{final} is the centroid position after full rest. The final value is averaged over the last 0.5 s frames to obtain the average final position after the particle has come to complete rest. Since particle density (steel 7850 kg/m^3, titanium 4500 kg/m^3) is significantly higher than liquid density (1051–1137 kg/m^3) and bed particle density (1250 kg/m^3), particles settle inside the bed, yielding $D > 0$.

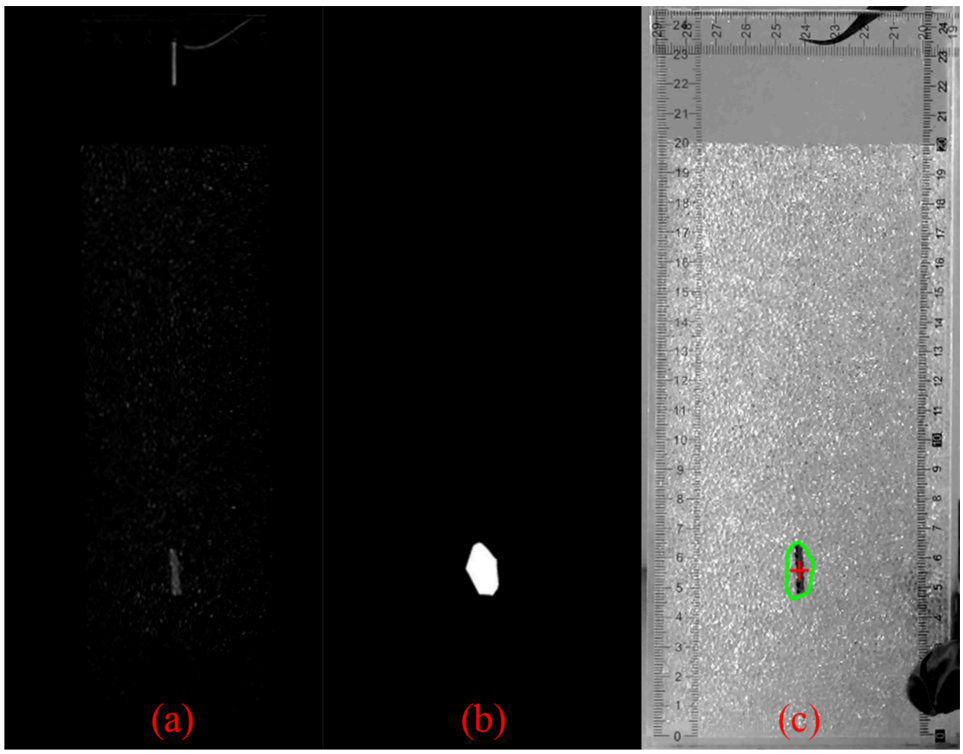


Figure 3. Image-processing procedure for extracting the position of the cylindrical intruder. (**a**) Background-corrected grayscale image after removing invalid regions outside the region of interest. (**b**) The binary region represents the segmented particle area used for centroid extraction rather than the exact geometric shape of the cylindrical intruder. (**c**) Final detection result superimposed on the original frame, where the green contour indicates the detected boundary of the binary particle region after thresholding and morphological processing, and the red cross indicates the calculated centroid position.

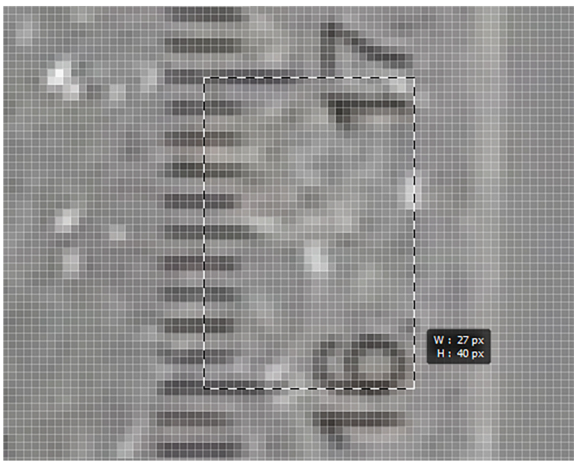


Figure 4. Schematic illustration of the image spatial calibration method.

The uncertainties in Z_{bed}, Z_{final}, and the calculated immersion depth (D) for a single trial are mainly associated with image calibration, bed-surface identification, and centroid extraction. Based on the calibrated image scale and repeated frame-by-frame checking, the single-trial uncertainty of these three quantities is controlled within ± 0.1 cm. The reported uncertainty in final immersion depth is further evaluated from three repeated tests and is expressed as the standard deviation.

The dimensionless displacement is defined as:

$$Z = \frac{Z_{\text{bed}} - Z_{\text{a}}}{d_{\text{b}}} \tag{4}$$

where Z_{a} is centroid position at any time. When $Z_{\text{a}} = Z_{\text{final}}$, Z equals the nondimensional final immersion depth $\frac{D}{d_{\text{b}}}$.

In addition, an intruder-based equivalent-volume Archimedes number is introduced to characterize the relative importance of gravitational driving force and viscous resistance during the motion of intruding particles in liquid-saturated beds [16,17]:

$$Ar = \frac{g d_{\text{i}}^3 \rho_{\text{l}} (\rho_{\text{i}} - \rho_{\text{l}})}{\eta^2} \tag{5}$$

where g is the gravitational acceleration, d_{i} is the equivalent intruder particle diameter, ρ_{i} and ρ_{l} are the densities of the intruder particle and liquid, respectively, and η is the dynamic viscosity of the liquid. Since all intruders investigated in this study are cylindrical particles, the equivalent diameter is calculated based on the equal-volume principle to account for differences in intruder length and aspect ratio.

For cylindrical particles, the equivalent diameter is calculated based on the equal-volume principle:

$$d_{\text{i}} = \left(\frac{3}{2} d_{\text{a}}^2 l_{\text{a}} \right)^{1/3} \tag{6}$$

where d_{a} and l_{a} are the diameter and length of the cylindrical intruder particle, respectively. This definition allows cylindrical particles with different aspect ratios to possess different characteristic length scales, thereby avoiding the limitation of the conventional diameter-based Archimedes number, in which cylindrical particles with identical diameters but different lengths would exhibit the same Ar value [18].

Through nondimensionalization, immersion curves under different viscosities (3.10–8.55 mPa·s) and bed geometries (spherical and cylindrical particles) can be compared in a unified coordinate system, revealing intrinsic effects of particle density, aspect ratio, and fluid properties on immersion depth and dynamics.

3. Results and Discussion

3.1. Summary of Dimensionless Immersion Depths

The experiments described in Sections 3.2–3.4 are conducted with initial solid volume fractions of approximately ($\varphi = 0.590 \pm 0.012$) for the spherical particle bed and ($\varphi = 0.543 \pm 0.011$) for the cylindrical particle bed. The effect of changing (φ) is discussed separately in Section 3.5. Here follows a systematic overview of our experimental data in terms of immersion depth of the intruders.

3.2. Effects of Liquid Viscosity and Density on Immersion Depth

Figure 5 compares the effect of liquid viscosity on the dimensionless immersion depth for representative steel and titanium intruders with different sizes in a cylindrical particle bed. The three liquids compared in this figure have nearly similar liquid density but different viscosities. The results indicate that the influence of viscosity depends on intruder conditions rather than exhibiting an identical trend for all cases. Although increasing viscosity leads to a higher immersion depth for some selected intruder conditions, other cases show weaker or non-monotonic variations.

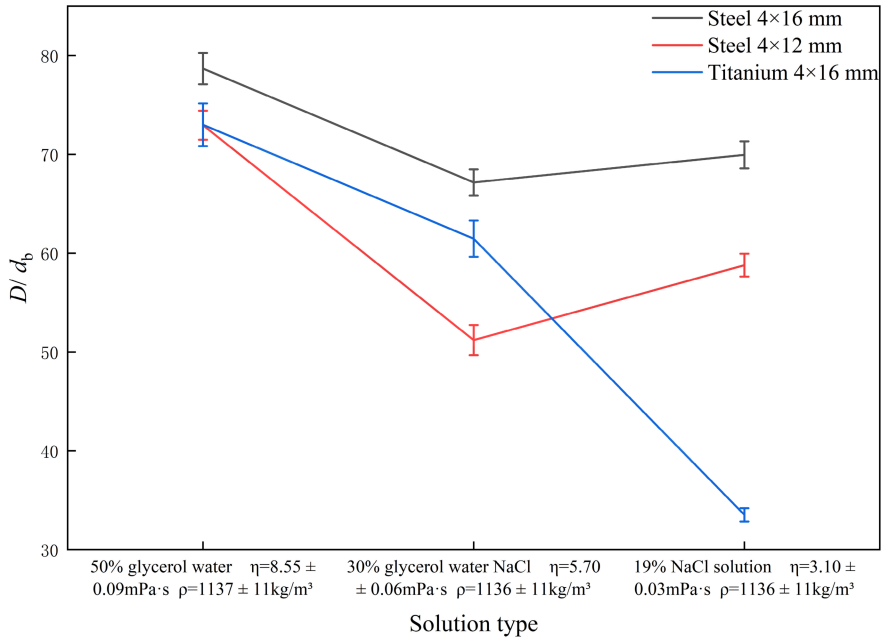


Figure 5. Dimensionless immersion depth as a function of liquid viscosity for representative steel and titanium intruders with different sizes in a cylindrical particle bed.

This trend is counterintuitive, because higher liquid viscosity is usually expected to increase viscous resistance during particle motion [19,20]. A similar increase in immersion depth with increasing liquid viscosity was previously observed by Li et al. for cylindrical intruders in liquid-saturated spherical particle beds [11]. Under the present experimental condition, however, the result indicates that viscosity may not act only as a resistance factor. It may also influence immersion through interfacial lubrication or by altering the dynamic response of the particle bed [21]. Derksen's lattice Boltzmann method–immersed boundary method (LBM–IBM) simulation suggests that viscous effects may become more significant at small interparticle spacings. Viscosity may also change energy dissipation during impact, thereby affecting the subsequent settling and immersion process [22,23].

Figure 6 compares the dimensionless immersion depths of steel intruders with different sizes in a cylindrical particle bed under two liquids with similar viscosity but different density and composition. The figure shows that the 50% glycerol–water solution produces greater immersion depths than the PEG aqueous solution under the same bed and intruder conditions. Since the two liquids have comparable viscosity, this difference cannot be explained by viscosity alone. One possible explanation is related to the difference in liquid density, which may influence the settling behavior of the saturated particle bed during bed preparation. The density difference between the bed particles and liquid is smaller in the 50% glycerol–water solution than in the PEG solution, which may reduce the effective settling tendency of bed particles and potentially influence the local packing structure. Although the measured solid volume fractions of the two saturated beds are comparable, the difference may be associated with liquid-density-dependent settling behavior during bed preparation, which could influence the local packing arrangement and pore-scale resistance. Therefore, the comparison in Figure 6 suggests that liquid density and liquid–particle coupling effects should be considered when interpreting immersion behavior, rather than attributing the observed difference only to viscosity.

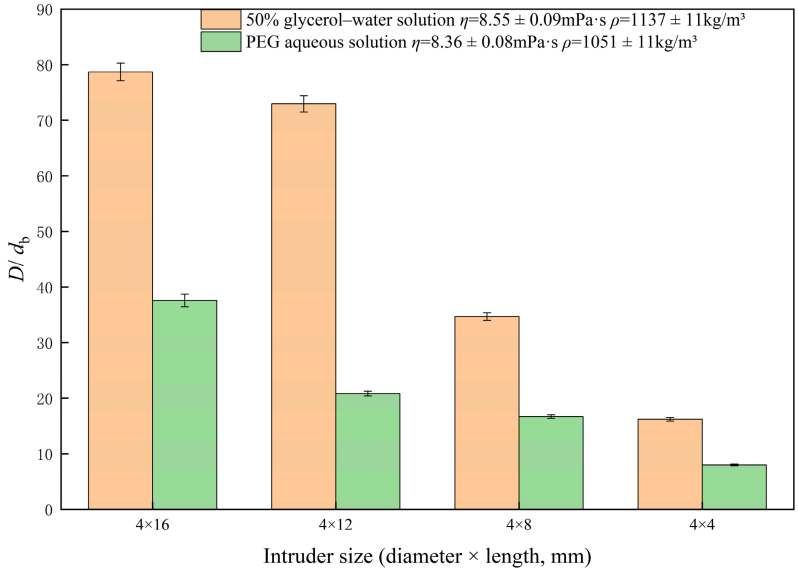


Figure 6. Dimensionless immersion depth in different solutions for steel intruders with different sizes in a cylindrical particle bed.

To further examine whether the observed liquid-property effects are limited to steel intruders, Figure 7 presents the corresponding results for titanium intruders with different sizes under the same liquid conditions. Similar differences between PEG aqueous solution and 50% glycerol–water solution are also observed for titanium intruders, suggesting that liquid-property effects are not limited to steel intruders.

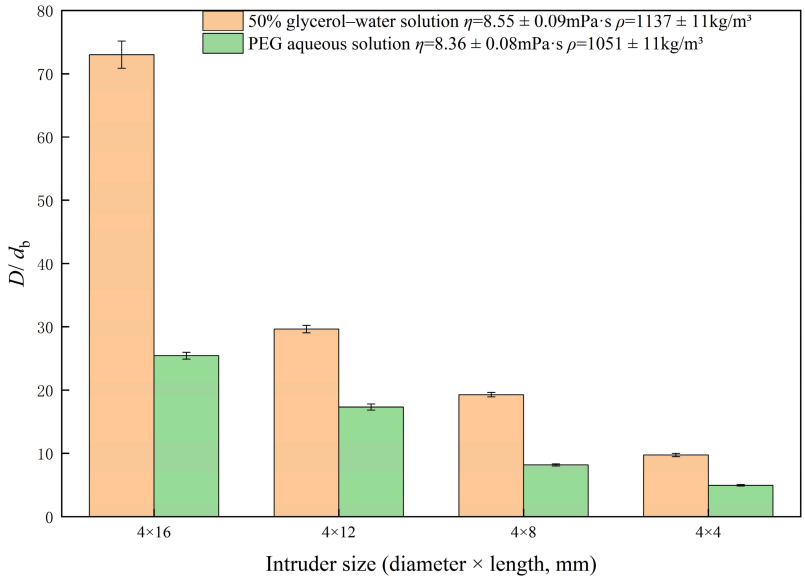


Figure 7. Dimensionless immersion depth in different solutions for titanium intruders with different sizes in a cylindrical particle bed.

Examination of the results in Tables 4–7 further indicates that the effects of liquid viscosity and density depend on the specific intruder properties and bed conditions. Although increasing viscosity promotes deeper immersion under some selected conditions, opposite or non-monotonic responses are also observed for other combinations of intruder size, material, and particle-bed morphology. Therefore, the influence of liquid properties should be understood as a condition-dependent response resulting from the interaction among liquid characteristics, intruder properties, and particle-bed systems.

Table 4. Dimensionless immersion depths in PEG aqueous solution (η = 8.36 ± 0.08 mPa·s; ρ = 1051 ± 11 kg/m^3). Values are mean ± standard deviation (SD) (n = 3).

Bed Morphology	Intruder Material	4 × 16	4 × 12	4 × 8	4 × 4
Spherical particle bed	Steel	75.60 ± 1.50	25.75 ± 0.50	19.65 ± 0.40	9.30 ± 0.20
Spherical particle bed	Titanium	14.35 ± 0.30	8.60 ± 1.05	7.40 ± 0.15	4.45 ± 0.10
Cylindrical particle bed	Steel	37.58 ± 1.11	20.84 ± 0.42	16.68 ± 0.32	8.00 ± 0.16
Cylindrical particle bed	Titanium	25.42 ± 0.53	17.32 ± 0.47	8.16 ± 0.16	4.95 ± 0.11

Table 5. Dimensionless immersion depths in 19% NaCl solution (η = 3.10 ± 0.03 mPa·s; ρ = 1136 ± 11 kg/m^3). Values are mean ± SD (n = 3).

Bed-Particle Morphology	Intruder Material	4 × 16	4 × 12	4 × 8	4 × 4
Spherical particle bed	Steel	77.35 ± 2.30	37.90 ± 1.15	27.45 ± 0.55	15.30 ± 0.30
Spherical particle bed	Titanium	34.10 ± 1.00	19.95 ± 0.40	10.75 ± 0.20	8.40 ± 0.15
Cylindrical particle bed	Steel	69.95 ± 1.37	58.79 ± 1.16	55.05 ± 1.63	23.58 ± 0.47
Cylindrical particle bed	Titanium	33.53 ± 0.68	26.26 ± 0.79	15.58 ± 0.32	10.89 ± 0.21

Table 6. Dimensionless immersion depths in 50% glycerol–water solution (η = 8.55 ± 0.09 mPa·s; ρ = 1137 ± 11 kg/m^3). Values are mean ± SD (n = 3).

Bed-Particle Morphology	Intruder Material	4 × 16	4 × 12	4 × 8	4 × 4
Spherical particle bed	Steel	76.40 ± 1.50	65.70 ± 1.30	24.85 ± 0.50	10.95 ± 0.30
Spherical particle bed	Titanium	25.80 ± 0.50	17.90 ± 0.35	14.10 ± 0.40	7.35 ± 0.15
Cylindrical particle bed	Steel	78.68 ± 1.58	72.95 ± 1.47	34.68 ± 0.68	16.21 ± 0.32
Cylindrical particle bed	Titanium	73.00 ± 2.16	29.63 ± 0.58	19.26 ± 0.37	9.74 ± 0.26

Table 7. Dimensionless immersion depths in 30% glycerol–water–NaCl solution (η = 5.70 ± 0.06 mPa·s; ρ = 1136 ± 11 kg/m^3). Values are mean ± SD (n = 3).

Bed-Particle Morphology	Intruder Material	4 × 16	4 × 12	4 × 8	4 × 4
Spherical particle bed	Steel	74.45 ± 1.50	56.35 ± 1.70	20.75 ± 0.40	14.40 ± 0.30
Spherical particle bed	Titanium	15.70 ± 0.45	12.30 ± 0.35	9.45 ± 0.25	4.60 ± 0.15
Cylindrical particle bed	Steel	67.16 ± 1.32	51.21 ± 1.53	20.95 ± 0.42	16.16 ± 0.32
Cylindrical particle bed	Titanium	61.47 ± 1.84	19.95 ± 0.37	13.89 ± 0.42	2.95 ± 0.05

3.3. Effects of Different Particle-Bed Systems on Intrusion Behavior

Previous experiments by Li et al. on liquid-saturated spherical particle beds show that cylindrical intruders generally penetrate deeper at higher liquid viscosity [11]. Building on this spherical-bed baseline, the present study further introduces cylindrical bed particles to examine whether bed-particle morphology affects immersion depth and its response to liquid properties.

Figure 8 compares the dimensionless immersion depths of steel intruders with different sizes in spherical and cylindrical particle beds under the 50% glycerol–water solution. For the selected 4 mm × 8 mm steel intruder case, the cylindrical bed gives a larger dimensionless immersion depth than the spherical bed. This may be related to the larger contact area and stronger packing anisotropy of cylindrical particles [24], which could change the local resistance encountered during immersion.

Figure 9 further compares the dimensionless immersion depth of a 4 mm × 12 mm steel intruder in the two bed morphologies under different liquid-viscosity conditions. For both spherical and cylindrical beds, the dimensionless immersion depth is larger under the higher-viscosity condition than under the lower-viscosity condition. This trend in the spherical bed

is consistent with the previous experimental observations reported by Li et al. for liquid-saturated spherical particle beds [11]. Under the selected lower-viscosity condition, the spherical bed gives a larger dimensionless immersion depth than the cylindrical bed. Under the higher-viscosity condition, the cylindrical bed gives a slightly larger dimensionless immersion depth than the spherical bed. These observations suggest that the relative difference between spherical and cylindrical beds may be influenced by liquid viscosity. The morphology–viscosity relation may be interpreted in terms of the competition between lubrication and friction effects suggested in Derksen's simulations [10].

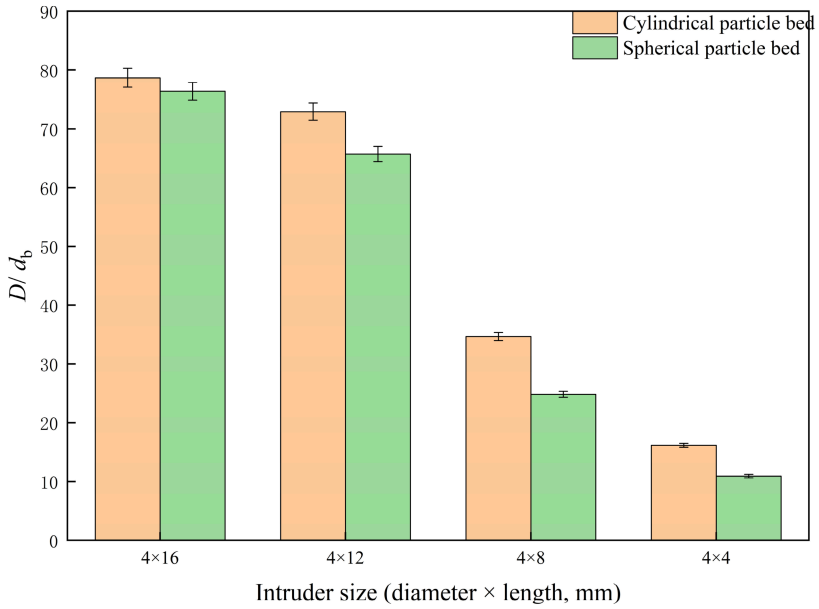


Figure 8. Dimensionless immersion depth of steel intruders with different sizes in spherical and cylindrical particle beds under 50% glycerol–water solution.

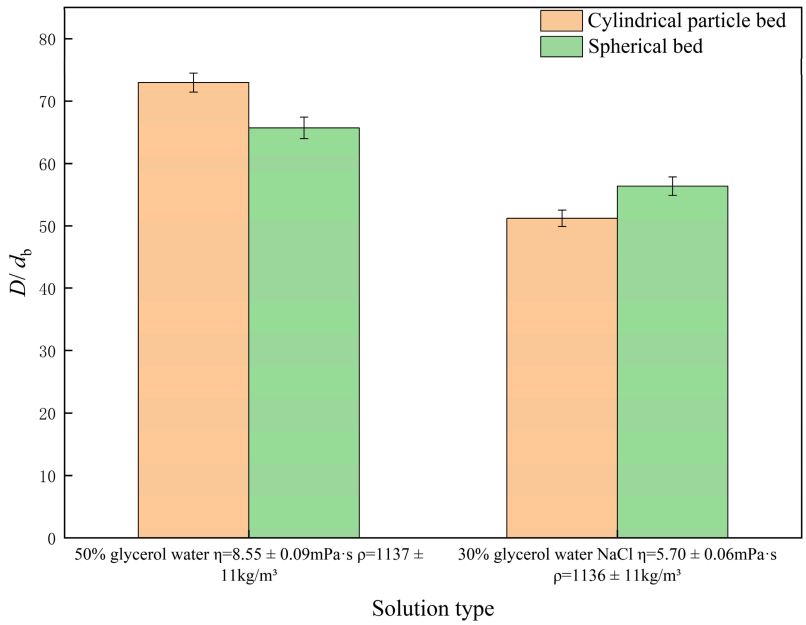


Figure 9. Dimensionless immersion depth as a function of liquid viscosity for a 4 mm × 12 mm steel intruder in different particle beds.

3.4. Intruder Density and Aspect Ratio

The effects of intruder material and aspect ratio are then analyzed using the immersion-depth data summarized in Tables 4–7. With bed structure and liquid properties unchanged, steel intruders show much greater dimensionless immersion depth than titanium intruders [25,26]. Under the 50% glycerol–water solution and cylindrical-bed condition, a 4 mm × 8 mm steel intruder reaches a dimensionless immersion depth of 34.7, whereas the same-sized titanium intruder reaches only 19.3.

When intruder material density remains constant, dimensionless immersion depth generally increases with particle aspect ratio. As shown in Figure 10, this trend is observed for steel intruders with different sizes under the tested conditions. To further examine whether this size-dependent behavior is limited to steel intruders, Figure 11 presents the corresponding results for titanium intruders. Similar increasing trends with aspect ratio are observed for titanium intruders, indicating that the influence of intruder size is not restricted to a specific intruder material.

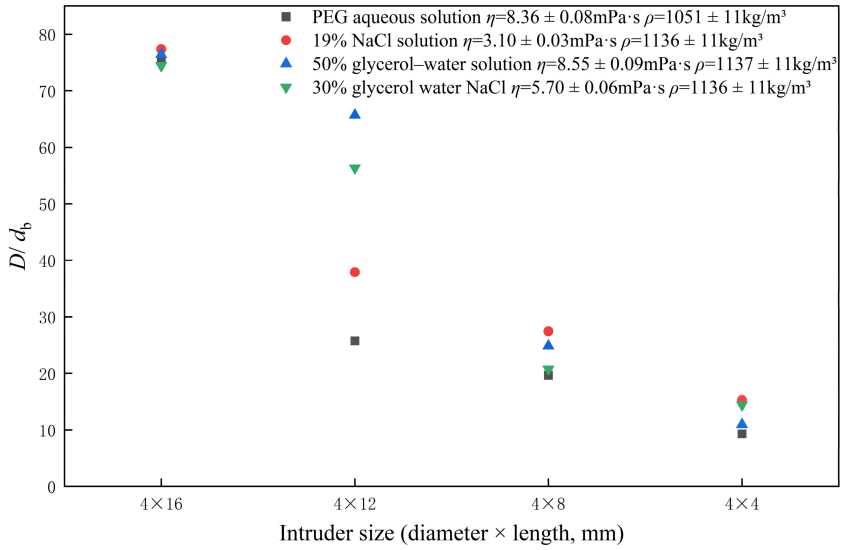


Figure 10. Dimensionless immersion depth of steel intruders with different sizes in a spherical particle bed under different liquid viscosities.

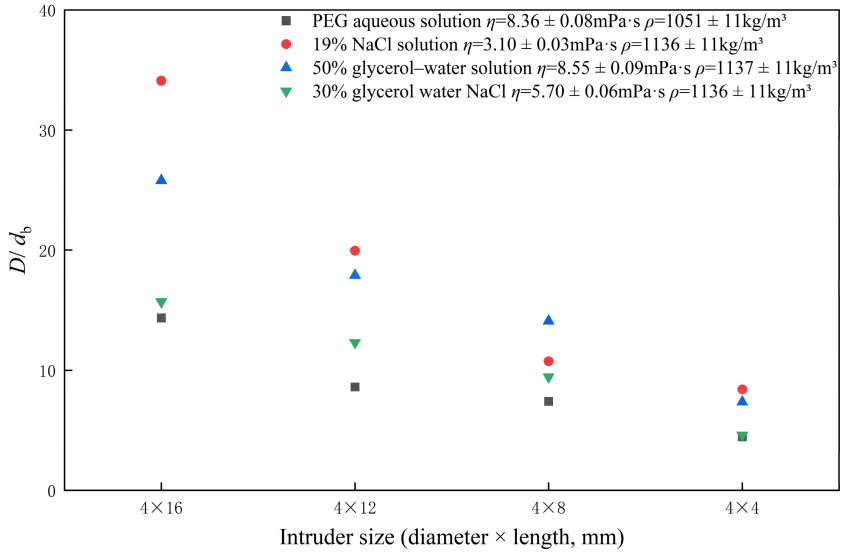


Figure 11. Dimensionless immersion depth of titanium intruders with different sizes in a spherical particle bed under different liquid viscosities.

The increase in dimensionless immersion depth with increasing intruder aspect ratio is most evident in the spherical bed with 19% NaCl solution: the 4 mm × 4 mm steel intruder reaches a dimensionless immersion depth of 15.3, while the 4 mm × 16 mm intruder of the same material reaches 77.4, nearly a fivefold increase, as shown in Figure 10. The relatively large spread observed for the 4 mm × 12 mm intruder may indicate a transitional immersion response, in which the intruder is more sensitive to local heterogeneity of the bed-particle skeleton and to slight variations in initial orientation or deflection during impact. This result indicates that increasing the aspect ratio enhances the immersion capability of the intruder, which is consistent with the increased gravitational driving force and inertia associated with a larger intruder mass [14,27].

3.5. Effect of Solid Volume Fraction

Previous studies show that changes in packing conditions can modify the solid volume fraction and the mechanical stability of jammed granular assemblies [28–30]. Therefore, additional comparison tests are performed to experimentally investigate how changes in the initial bed solid volume fraction influence the immersion behavior of intruders.

Using a cylindrical particle bed, PEG aqueous solution, and a 4 mm × 8 mm steel intruder as fixed conditions, two initial packing states are compared. Figure 12 presents the immersion trajectory of the vibration-compacted particle bed, where the initial solid volume fraction increases to $\varphi = 0.557 \pm 0.011$ and the final dimensionless immersion depth is 10.8 ± 0.3. In comparison, Figure 13 shows the immersion trajectory obtained from the naturally settled particle bed with $\varphi = 0.543 \pm 0.011$, where the final immersion depth reaches 16.7 ± 0.3. Since the compacted bed was obtained by further compacting the naturally settled bed under the same experimental conditions, the particle mass, particle density, and container geometry remained unchanged between the two states. Therefore, the uncertainty associated with the difference in solid volume fraction between the naturally settled and compacted beds is mainly determined by the uncertainty of the measured bed-height variation.

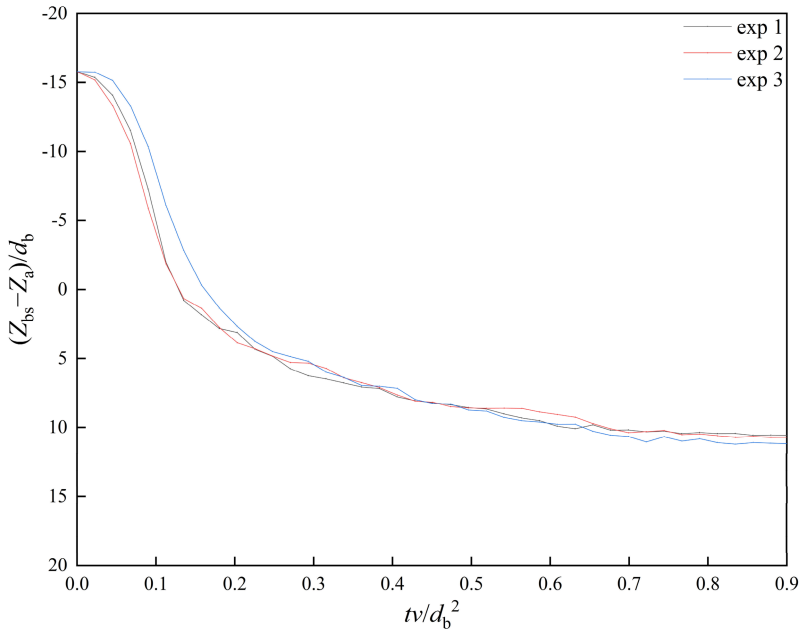


Figure 12. Dimensionless immersion trajectories of a 4 mm × 8 mm steel intruder in a vibration-compacted cylindrical particle bed saturated with PEG aqueous solution ($\varphi = 0.557 \pm 0.011$). Three repeat experimental realizations are conducted under the same conditions.

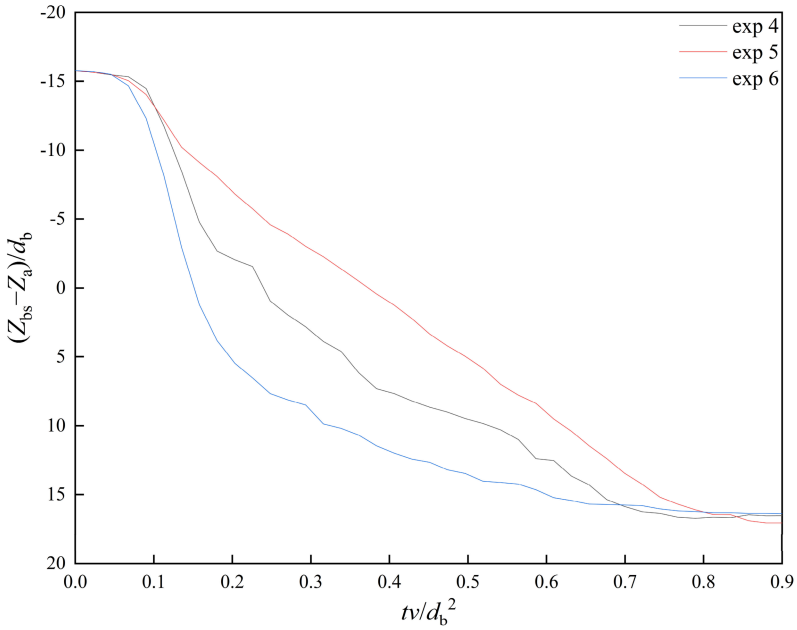


Figure 13. Dimensionless immersion trajectories of a 4 mm × 8 mm steel intruder in a naturally settled cylindrical particle bed saturated with PEG aqueous solution ($\varphi = 0.543 \pm 0.011$). Three repeat experimental realizations are conducted under the same conditions.

Somfai et al. report that near the jamming transition, a slight increase in φ can significantly enhance system rigidity [31]. In this experiment, when φ increases from 0.543 to 0.557, immersion depth decreases by about 35%. The result indicates that compaction increases the solid volume fraction, densifies the bed, and increases the overall resistance to intrusion. This behavior is consistent with the expectation that a more compacted granular assembly exhibits higher effective rigidity and reduced mobility [28].

Lattice Boltzmann numerical simulation has been applied to solid–liquid particulate systems. To further support the interpretation of the solid-volume-fraction effect, representative particle-resolved simulation results are included in Figure 14. The simulations follow the lattice-Boltzmann and immersed-boundary framework reported previously for cylindrical intruders in wet granular beds [11]. In the present simulations, PEG-saturated cylindrical particle beds were generated with different initial packing states. Each computational bed contained 3840 bed particles, with a bed width of 32 mm and an initial depth of 20 mm. The cylindrical bed particles had a diameter of 1.75 mm, a length of 1.50 mm, and a density of 1250 kg/m^3. A steel cylindrical intruder with a diameter of 4 mm and a length of 8 mm was selected to correspond to the representative experimental condition. By adjusting the bed packing state, the simulated solid volume fraction increased from $\varphi = 0.533$ to $\varphi = 0.552$.

The simulations show that increasing the solid volume fraction reduces the final dimensionless immersion depth from 10.1 to 3.7, indicating that bed compaction increases resistance to intrusion. Because the computational domain contains fewer particles and a smaller bed depth than the experimental system, the simulation results are not intended for quantitative comparison with experimental immersion depths. Instead, the simulations provide additional qualitative support that increasing solid volume fraction suppresses intruder immersion.

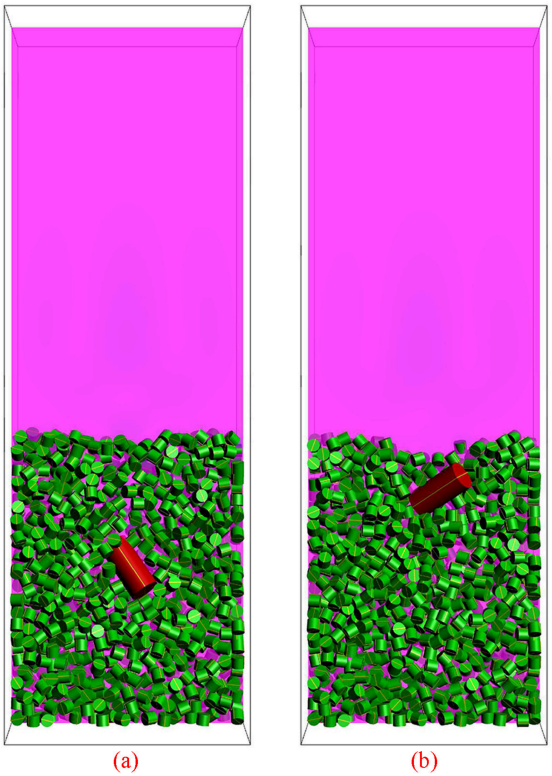


Figure 14. Particle-resolved simulation snapshots of a 4 mm × 8 mm steel intruder in PEG-saturated cylindrical particle beds at the final resting state. (**a**) Loosely settled bed with $\varphi = 0.533$, corresponding to a final dimensionless immersion depth of 10.1. (**b**) Compacted bed with $\varphi = 0.552$, corresponding to a final dimensionless immersion depth of 3.7. The red particle is the intruder, and the green particles show a cross-section of the cylindrical bed particles.

4. Conclusions

This study experimentally investigates the immersion behavior of steel and titanium cylindrical intruders in liquid-saturated spherical and cylindrical particle beds. The effects of intruder properties, liquid characteristics, particle-bed morphology, and solid volume fraction on dimensionless immersion depth are systematically examined.

First, intruder properties significantly influence immersion behavior. Under identical bed and liquid conditions, steel intruders generally exhibit larger dimensionless immersion depths than titanium intruders due to their higher density. Increasing the aspect ratio of intruders further enhances immersion depth, and this tendency is observed for both steel and titanium intruders.

Second, liquid properties affect immersion behavior in a condition-dependent manner. In some selected cases, increasing liquid viscosity results in larger dimensionless immersion depths, indicating that viscosity does not act only as a resistance factor during intrusion. However, other cases show weaker or non-monotonic variations, suggesting that viscosity effects depend on the interaction among liquid properties, intruder characteristics, and particle-bed conditions. In addition, comparisons between liquids with similar viscosity but different densities demonstrate that liquid density-related effects should also be considered.

Third, particle-bed morphology influences immersion behavior through its interaction with liquid conditions. The relative immersion depth between spherical and cylindrical particle beds is not constant: the spherical bed produces larger immersion depths under lower-viscosity conditions, whereas the cylindrical bed shows slightly larger values under higher-viscosity conditions. This indicates that bed morphology and liquid properties jointly determine the resistance experienced by intruders.

Finally, the initial solid volume fraction is an important parameter characterizing the packing state and resistance of the particle bed. Increasing the solid volume fraction through vibration compaction reduces the final immersion depth by increasing the resistance of the bed to intrusion. For the cylindrical bed saturated with PEG aqueous solution, vibration compaction increases the solid volume fraction from 0.543 ± 0.011 to 0.557 ± 0.011, accompanied by a reduction in dimensionless immersion depth from 16.7 ± 0.3 to 10.8 ± 0.3. This result indicates that variations in packing state should be considered when comparing immersion behavior under different bed conditions.

Overall, the final immersion depth in liquid-saturated heterogeneous particle beds is governed by the coupled effects of intruder properties, liquid characteristics, particle-bed morphology, and packing state rather than by a single controlling parameter. The present experiments extend previous spherical-particle-bed studies by introducing cylindrical bed particles and comparing the immersion behavior under different bed morphologies and liquid conditions. Future studies combining particle-scale simulations and advanced visualization techniques may further clarify the mechanisms underlying liquid-property effects and morphology-dependent immersion behavior.

Author Contributions: Conceptualization, K.L., L.Z. and J.J.D.; methodology, K.L., L.Z., J.L. and J.J.D.; software, K.L. and J.J.D.; validation, K.L., L.W., Y.X., M.T., P.G. and J.L.; formal analysis, K.L., L.Z., J.L. and J.J.D.; investigation, K.L., L.W., Y.X., M.T., P.G. and J.L.; resources, L.Z. and J.J.D.; data curation, K.L., L.W., Y.X., M.T., P.G. and J.L.; writing—original draft preparation, K.L.; writing—review and editing, L.Z., L.W., Y.X., J.L. and J.J.D.; visualization, K.L. and J.J.D.; supervision, L.Z. and J.J.D.; project administration, L.Z.; funding acquisition, L.Z. All authors have read and agreed to the published version of the manuscript.

Funding: This research was funded by the National Natural Science Foundation of China, grant numbers 22078191, 21978165, 22081340412 and 92156020.

Institutional Review Board Statement: Not applicable.

Informed Consent Statement: Not applicable.

Data Availability Statement: The raw data supporting the conclusions of this article will be made available by the authors on request.

Acknowledgments: We gratefully acknowledge the technical assistance provided by colleagues at Shanghai University of Engineering Science. During the preparation of this manuscript, we used ChatGPT (OpenAI, San Francisco, CA, USA, GPT-5.6) for language polishing, grammatical correction, and improving the readability of the text. All AI-assisted content was carefully reviewed and revised by the authors, who take full responsibility for the final content of this publication.

Conflicts of Interest: The authors declare no conflicts of interest.

References

1. Kamrin, K.; Hill, K.M.; Goldman, D.I.; Andrade, J.E. Advances in Modeling Dense Granular Media. *Annu. Rev. Fluid Mech.* **2024**, *56*, 215–240. [CrossRef]
2. Strader, J.; Causley, N.; Dijksman, J.A.; Clark, A.H. Darcy-Reynolds Forces during Intrusion into Granular-Fluid Beds. *Phys. Rev. Fluids* **2022**, *7*, 054304. [CrossRef]
3. Shin, C.H. Permeability Variation Analysis Using the Superficial Diameter Correlation with Porosity Change. *Phys. Fluids* **2021**, *33*, 053108. [CrossRef]
4. Zuñiga, R.; Job, S.; Santibanez, F. Effect of an Interstitial Fluid on the Dynamics of Three-Dimensional Granular Media. *Phys. Rev. E* **2019**, *99*, 032905. [CrossRef]
5. Van Der Meer, D. Impact on Granular Beds. *Annu. Rev. Fluid Mech.* **2017**, *49*, 463–484. [CrossRef]
6. Nelson, E.L.; Katsuragi, H.; Mayor, P.; Durian, D.J. Projectile Interactions in Granular Impact Cratering. *Phys. Rev. Lett.* **2008**, *101*, 068001. [CrossRef]

7. Wang, F.; Chen, Y.; Li, Y.; Li, Y. A Drag Force Model of Vertical Penetration into a Granular Medium Based on DEM Simulations and Experiments. *Appl. Sci.* **2024**, *14*, 2336. [CrossRef]
8. Marston, J.O.; Vakarelski, I.U.; Thoroddsen, S.T. Sphere Impact and Penetration into Wet Sand. *Phys. Rev. E* **2012**, *86*, 020301. [CrossRef]
9. Allen, B.; Kudrolli, A. Effective Drag of a Rod in Fluid-Saturated Granular Beds. *Phys. Rev. E* **2019**, *100*, 022901. [CrossRef]
10. Derksen, J.J. Settling of Heavy Cylindrical Particles in Granular Beds. *Int. J. Multiph. Flow* **2022**, *157*, 104232. [CrossRef]
11. Li, J.; Zhang, L.; Han, K.; Lin, S.; Lu, J.; Liu, F.; Derksen, J.J. Cylinders Intruding Wet Granular Beds—Experiment and Simulation. *J. Hydraul. Res.* **2024**, *62*, 351–364. [CrossRef]
12. Otsu, N. A Threshold Selection Method from Gray-Level Histograms. *IEEE Trans. Syst. Man Cybern.* **1979**, *9*, 62–66. [CrossRef]
13. Ruffin, C.; King, R.L. The Analysis of Hyperspectral Data Using Savitzky-Golay Filtering-Theoretical Basis. In Proceedings of the IEEE 1999 International Geoscience and Remote Sensing Symposium. IGARSS'99 (Cat. No. 99CH36293), Hamburg, Germany, 28 June–2 July 1999; Volume 2, pp. 756–758. [CrossRef]
14. Katsuragi, H.; Durian, D.J. Drag Force Scaling for Penetration into Granular Media. *Phys. Rev. E* **2013**, *87*, 052208. [CrossRef]
15. Ten Cate, A.; Nieuwstad, C.H.; Derksen, J.J.; Van Den Akker, H.E.A. Particle Imaging Velocimetry Experiments and Lattice-Boltzmann Simulations on a Single Sphere Settling under Gravity. *Phys. Fluids* **2002**, *14*, 4012–4025. [CrossRef]
16. Xie, J.; Zhang, L.; Lu, M.; Lu, J.; Derksen, J.J. Experiments and Simulations of Settling Cylinders over a Wide Range of Archimedes Numbers. *Can. J. Chem. Eng.* **2023**, *101*, 2240–2249. [CrossRef]
17. Hamidi, A.; Daramsing, D.; Gordon, M.D.; Hanson, R.E. Low Reynolds Number Settling of Bent Rods in Quiescent Fluid. *Fluids* **2026**, *11*, 72. [CrossRef]
18. Lu, M.; Zhang, L.; Li, J.; Lu, J.; Liu, F.; Derksen, J.J. Experiments on and Simulations of Hollow Cylinders Falling through Quiescent Liquids. *Chem. Eng. Technol.* **2024**, *47*, 596–604. [CrossRef]
19. Hossain, T.; Rognon, P. Drag Force in Immersed Granular Materials. *Phys. Rev. Fluids* **2020**, *5*, 054306. [CrossRef]
20. Lin, J.; Zhao, T.; Jiang, M. Drag Force Regime in Dry and Immersed Granular Media. *Phys. Rev. E* **2024**, *109*, 064908. [CrossRef]
21. Jareteg, A.; Maggiolo, D.; Sasic, S.; Ström, H. On the Roles of Interstitial Liquid and Particle Shape in Modulating Microstructural Effects in Packed-Bed Adsorbers. *Chem. Eng. Res. Des.* **2022**, *177*, 682–693. [CrossRef]
22. Lin, J.; Zhao, T.; Jiang, M. Investigating Projectile Penetration into Immersed Granular Beds via CFD-DEM Coupling. *Granul. Matter* **2023**, *25*, 77. [CrossRef]
23. Brzinski, T.A.; Schug, J.; Mao, K.; Durian, D.J. Penetration Depth Scaling for Impact into Wet Granular Packings. *Phys. Rev. E* **2015**, *91*, 022202. [CrossRef]
24. Derksen, J.J. Liquid Fluidization with Cylindrical Particles: Highly Resolved Simulations. *AIChE J.* **2019**, *65*, e16594. [CrossRef]
25. Kang, W.; Feng, Y.; Liu, C.; Blumenfeld, R. Archimedes' Law Explains Penetration of Solids into Granular Media. *Nat. Commun.* **2018**, *9*, 1101. [CrossRef]
26. Iikawa, N.; Katsuragi, H. Applicability of Extended Modified Archimedes' Law to Various Granular and Intruder Properties. *Comput. Part. Mech.* **2025**, *12*, 3371–3388. [CrossRef]
27. Li, P.; Li, Y.; Hua, X.; Guo, Y.; Curtis, J.S. 3D DEM Simulations and Experiments on Spherical Impactor Penetrating into the Elongated Particles. *Materials* **2023**, *16*, 1664. [CrossRef]
28. Gan, J.; Yu, A. DEM Simulation of the Packing of Cylindrical Particles. *Granul. Matter* **2020**, *22*, 22. [CrossRef]
29. Donev, A.; Cisse, I.; Sachs, D.; Variano, E.A.; Stillinger, F.H.; Connelly, R.; Torquato, S.; Chaikin, P.M. Improving the Density of Jammed Disordered Packings Using Ellipsoids. *Science* **2004**, *303*, 990–993. [CrossRef]
30. Torquato, S. Perspective: Basic Understanding of Condensed Phases of Matter via Packing Models. *J. Chem. Phys.* **2018**, *149*, 020901. [CrossRef]
31. Somfai, E.; Van Hecke, M.; Ellenbroek, W.G.; Shundyak, K.; Van Saarloos, W. Critical and Noncritical Jamming of Frictional Grains. *Phys. Rev. E* **2007**, *75*, 020301. [CrossRef]

Disclaimer/Publisher's Note: The statements, opinions and data contained in all publications are solely those of the individual author(s) and contributor(s) and not of MDPI and/or the editor(s). MDPI and/or the editor(s) disclaim responsibility for any injury to people or property resulting from any ideas, methods, instructions or products referred to in the content.